

Article

Integration of WO₃-Doped MoO₃ with ZnO Photocatalyst for the Removal of 2-Nitrophenol in Natural Sunlight Illumination

Sofia Mateen ¹, Rabia Nawaz ², Muhammad Tariq Qamar ^{1,*}, Shahid Ali ³ , Shahid Iqbal ^{2,*} ,
Muhammad Aslam ⁴, Muhammad Raheel ⁵, Nasser S. Awwad ⁶  and Hala A. Ibrahim ⁷

¹ Department of Chemistry, Forman Christian College (A Chartered University), Ferozepur Road, Lahore 54600, Pakistan

² Department of Chemistry, School of Natural Sciences (SNS), National University of Science and Technology (NUST), H-12, Islamabad 46000, Pakistan

³ Interdisciplinary Research Center for Hydrogen and Energy Storage (IRC-HES), King Fahd University of Petroleum and Minerals (KFUPM), Dhahran 31261, Saudi Arabia

⁴ Centre of Excellence in Environmental Studies (CEES), King Abdulaziz University, Jeddah 21589, Saudi Arabia

⁵ Department of Chemistry, Balochistan University of Information Technology, Engineering and Management Sciences, Quetta 87300, Pakistan

⁶ Chemistry Department, Faculty of Science, King Khalid University, P.O. Box 9004, Abha 61413, Saudi Arabia

⁷ Biology Department, Faculty of Science, King Khalid University, P.O. Box 9004, Abha 61413, Saudi Arabia

* Correspondence: tariqqamar@fccollege.edu.pk (M.T.Q.); shahidiqbal.chem@sns.nust.edu.pk (S.I.)

Abstract: Environmental contamination has become the most pressing issue in recent years. The value of clean water to mankind has sparked interest in heterogeneous photocatalysis. In this study, a novel photocatalyst has been synthesized by integrating WO₃-doped MoO₃ (WDM) and ZnO through composite formation. The composite nature of the synthesized photocatalyst was confirmed due to the presence of hexagonal ZnO and orthorhombic WDM phases in XRD pattern and scanning electron micrographs. Solid-state absorption spectra and a bandgap analysis showed that WDM-spectral ZnO's response was better than that of pure ZnO. PL and EIS unveiled the effective role of WDM in suppressing the $e^- - h^+$ recombination process and charge-transfer resistance, respectively, in ZnO. The photocatalytic studies showed that WDM-ZnO was able to remove ~90% of 30 ppm 2-nitrophenol (2-NP) with a rate of $1.1 \times 10^{-2} \text{ min}^{-1}$, whereas ~65% 2-NP was removed by ZnO ($6.1 \times 10^{-3} \text{ min}^{-1}$ rate) under the exposure of natural sunlight ($800 \times 10^2 \pm 100 \text{ lx}$). Moreover, ~52% higher total organic carbon (TOC) removal was observed by WDM-ZnO as compared to ZnO. The photocatalytic removal of 2-NP by the produced photocatalysts followed the Langmuir-Hinshelwood kinetic model, as shown by the kinetic studies. The reactive oxygen species (ROS)-trapping established that the photocatalytic removal mechanism of 2-NP over WDM-ZnO in sunlight illumination was mainly triggered by the superoxide anion ($\text{O}_2^{\bullet-}$) radical, however, the minor role of hydroxyl ($\bullet\text{OH}$) radicals cannot be completely ignored.

Keywords: sunlight photocatalysis; WDM-ZnO; 2-nitrophenol; TOC removal



Citation: Mateen, S.; Nawaz, R.; Qamar, M.T.; Ali, S.; Iqbal, S.; Aslam, M.; Raheel, M.; Awwad, N.S.; Ibrahim, H.A. Integration of WO₃-Doped MoO₃ with ZnO Photocatalyst for the Removal of 2-Nitrophenol in Natural Sunlight Illumination. *Catalysts* **2023**, *13*, 1262. <https://doi.org/10.3390/catal13091262>

Academic Editors: Hongxing Dai and Jorge Bedia

Received: 15 July 2023

Revised: 12 August 2023

Accepted: 28 August 2023

Published: 31 August 2023



Copyright: © 2023 by the authors. Licensee MDPI, Basel, Switzerland. This article is an open access article distributed under the terms and conditions of the Creative Commons Attribution (CC BY) license (<https://creativecommons.org/licenses/by/4.0/>).

1. Introduction

The global battle against the contamination of the environment is the most significant task in this century. Water contamination is the biggest concern as a result of the many different forms of environmental degradation that the world is presently experiencing. Although chemical-based businesses play a significant role in human civilization, countless anthropogenic and industrial activities have released enormous quantities of chemicals into the environment, possibly affecting a wide range of ecosystems [1]. The recent growth of the textile, paint, leather, plastics, food, and cosmetics sectors is linked to the release of several organic pollutants that are detrimental to human health, aquatic systems, and microorganisms [2,3]. In addition, key aspects of the discharged water, such as toxicity,

biochemical oxygen demand, chemical oxygen demand, unpleasant odor, and color, may alter because of the influence of these organic effluents in wastewater. Effluent may become colored by even a small quantity of colorful organic molecules in the aquatic system. Because tinted water makes it more difficult for aquatic life and plants to obtain sunlight, it has a detrimental effect on the ecosystem by limiting photosynthesis. Consequently, color removal and sanitization have turned into ecological issues and are essential for maintaining the ecosystem [4,5].

Phenolic derivatives in wastewater sources have recently attracted much concern due to their toxicity. Nitrophenol derivatives are regarded as the largest contaminant of industrial wastewater due to their application in a number of chemical industries. The massive use of these nitrophenols as a result of growing urbanization and globalization has led to an excessive discharge of these pollutants into water bodies, creating a number of environmental problems [6]. 2-nitrophenol (2-NP) is one of the most hazardous and long-lasting organic contaminants found in industrial effluent and due to high water solubility, intense color, stability, and resistance to degradation has attracted particular attention [7,8]. The USEPA has declared 2-NP as a priority pollutant and has recommended its concentration in natural waterways be limited to less than 5 ppb. Therefore, the removal of 2-NP is highly desirable.

Due to the complexity and wide range of organic compounds utilized, it has become difficult to find a single treatment approach that entirely covers the effective removal of all these organic contaminants. The removal of these contaminants from wastewater has historically been accomplished using a variety of conventional or traditional wastewater treatment techniques, such as biological, physical, and chemical cleaning. However, traditional water treatment systems have been found to be unable to completely degrade organic toxins in aqueous system [9]. The low cost and convenience of use are the advantages of biological therapy, but the results are often subpar because of the considerable resistance to aerobic biodegradation [10]. The physical processes of flocculation, precipitation, granular activated carbon (GAC), and reverse osmosis are all used to extract phenols (RO). In most cases, physical therapy is successful in eliminating dyes, but the post-treatment care is challenging [11]. Other drawbacks of chemical treatment include the creation of hazardous byproducts, the need for high chemical dosages, and incomplete disintegration [12].

Due to the shortcomings of current wastewater treatment systems, it is essential to design a significantly improved wastewater treatment technology. In this context, photocatalytic water decontamination methods using a natural light source, i.e., sunlight, has received considerable attention due to their green approach and the formation of benign products without leaving toxic content after the degradation process [13,14]. This has been shown to be a viable alternative to traditional wastewater treatment for removing organic contaminants from a variety of industrial waste [15]. When a photocatalyst is stimulated by light, ROS are produced. ROS also convert organic toxins into harmless molecules [16]. In this context, various metal oxides such as TiO_2 , ZnO , CeO_2 , Fe_2O_3 , SnO_2 , Bi_2O_3 , etc., have been used as photocatalysts for the removal of organic pollutants [17].

Among metal oxides, ZnO is extensively used as a photocatalyst because of its low cost, tunable bandgap, n-type nature, natural abundance, and non-toxicity. However, its wide application is limited because of its high bandgap energy (~3.3 eV), which lies in the UV region of the light spectrum, low photonic yield, and high electron-hole pair recombination rate [18]. It utilizes only ~5% of sunlight, i.e., the UV portion, however, it cannot harvest the visible portion (~45%) of natural sunlight due to its wide bandgap [19]. Due to these restrictions, researchers now have a new area of inquiry, how to broaden or move the ZnO absorption spectrum from the UV to the visible range. According to several studies, ZnO 's photocatalytic activity can be enhanced by improving the spectral response and lowering of the charge recombination rate. These problems related to ZnO can only be accomplished by modifying ZnO through doping or composite formation [20,21].

In this study, hexagonal ZnO has been modified with WO_3 -doped MoO_3 using composite formation, since tungsten oxide and molybdenum oxide have comparable ionic

radii and electronic structures, and tungsten oxide is a natural option for molybdenum oxide doping in order to produce a doped oxide in the host oxide. This makes it easy to incorporate W^{6+} into the crystalline lattice of molybdenum oxide. Phuruangrat et al. successfully synthesized W-doped MoO_3 using a hydrothermal method and reported its excellent chemical stability, reusability, and photocatalytic activity for the removal of methylene blue (MB) dye [22]. Moreover, these oxides are essential components for a wide range of crucial applications, including solar energy materials and smart window technologies as well as electrical devices including photoelectrodes, organic electronics, sensors, and optical devices [23]. These above-mentioned properties have encouraged us to utilize WO_3 -doped MoO_3 to enhance the photocatalytic activity of ZnO for wastewater treatment. The WDM-ZnO and pristine ZnO photocatalysts were characterized using DRS, PL, XRD, and SEM for optical, structural, and morphological evaluation. Under irradiation with natural sunlight, a photocatalytic experiment was carried out to remove 30 ppm 2-NP from the synthesized photocatalysts, and the removal of organic content was determined using a TOC analyzer. The charge-transfer resistance posed by the materials was assessed through a Nyquist plot. Moreover, the contribution of ROS in the photocatalytic removal of 2-NP by WDM-ZnO was also estimated to establish the photocatalytic mechanism.

2. Results and Discussion

The XRD measurements of MoO_3 , WO_3 , and WO_3 -doped MoO_3 (WDM) are provided in Figure 1a. The main reflections owing to pure MoO_3 and WO_3 were in accordance with orthorhombic MoO_3 (JCPDS#05-0508) and monoclinic WO_3 (JCPDS#43-1035), respectively [24–26]. In WDM, a minor peak shift towards a lower diffraction angle and a decrease in the peak intensities of the preferred planes (021) and (020) of MoO_3 were noticed, as presented in Figure 1b,c. Whereas peaks related to the presence of WO_3 in the structure were also observed. The major peaks' variation, either in position or intensity, reveals the incorporation of W^{6+} into the structure of MoO_3 [27]. Moreover, the presence of major reflections due to hexagonal ZnO (JCPDS# 36-1451) and the newly synthesized WDM in the XRD pattern of WDM-ZnO confirm the formation of the composite, as shown in Figure 2. The presence of hexagonal ZnO and orthorhombic-like WDM in the SEM images as shown in Figure 3 serves as further evidence of the synthesized photocatalyst's composite nature. The microstructural parameters such as crystallite size (D), interplanar distance (d), dislocation density (δ), micro-strain (ϵ), and stacking fault (SF) of the synthesized materials were calculated using Equations (1)–(4) and are presented in Table 1. Using the Debye–Scherrer equation shown below, the crystallite size (D) was determined [28]:

$$D = \frac{K\lambda}{\beta \cos \theta} \quad (1)$$

where K is a shape factor and the Scherrer constant, β is the full width at half maximum (FWHM), λ is the X-ray wavelength, and θ is the Bragg diffraction angle. The dislocation density (δ) was calculated using the following equation [28]:

$$\delta = \frac{1}{D^2} \quad (2)$$

where δ and D are the dislocation density and crystallite size (nm), respectively. Furthermore, the following equations were used to compute the micro-strain (ϵ) and stacking fault (SF) [29].

$$\epsilon = \frac{\beta \cos \theta}{4} \quad (3)$$

$$SF = \frac{2\pi^2 \times \beta}{45 \times \sqrt{3} \tan \theta} \quad (4)$$

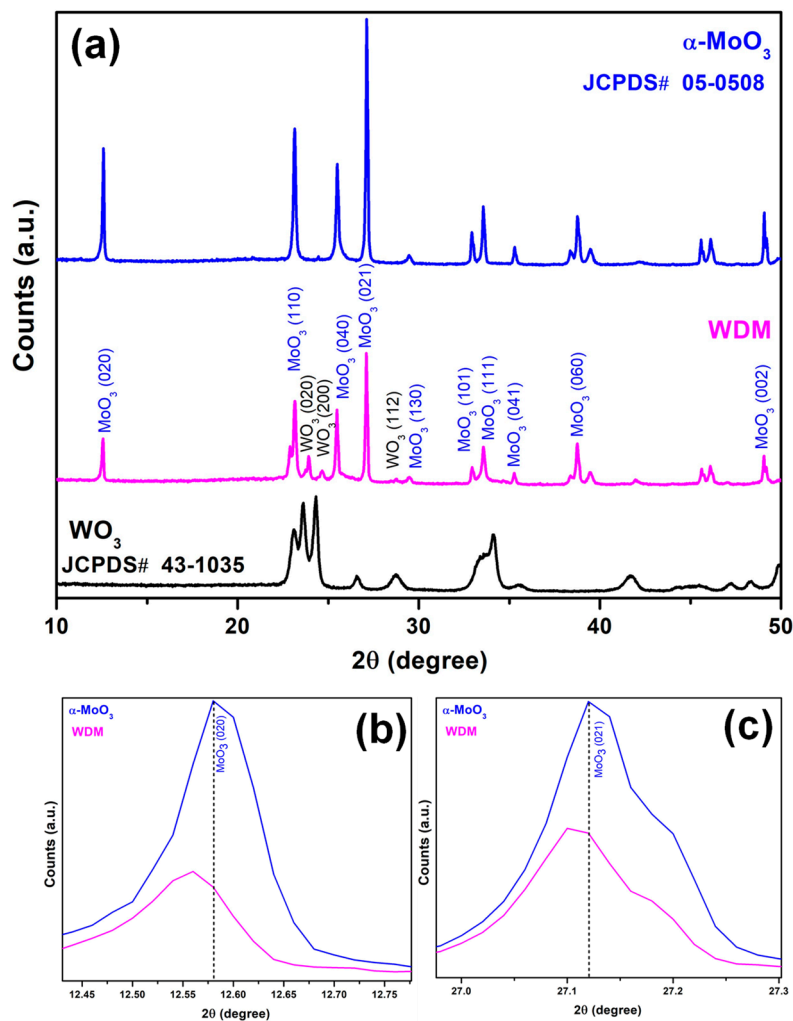


Figure 1. Comparing XRD pattern types of (a) WO_3 , MoO_3 , and WDM (WO_3 -doped MoO_3). (b,c) Represent peak shifting of (020) and (021) planes of MoO_3 in WDM.

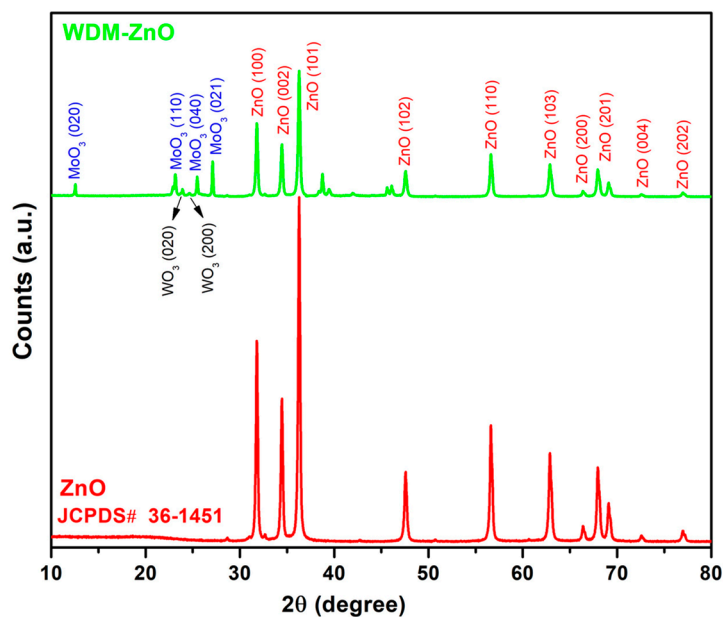


Figure 2. Comparing XRD pattern types of pure ZnO and WDM-ZnO composite.

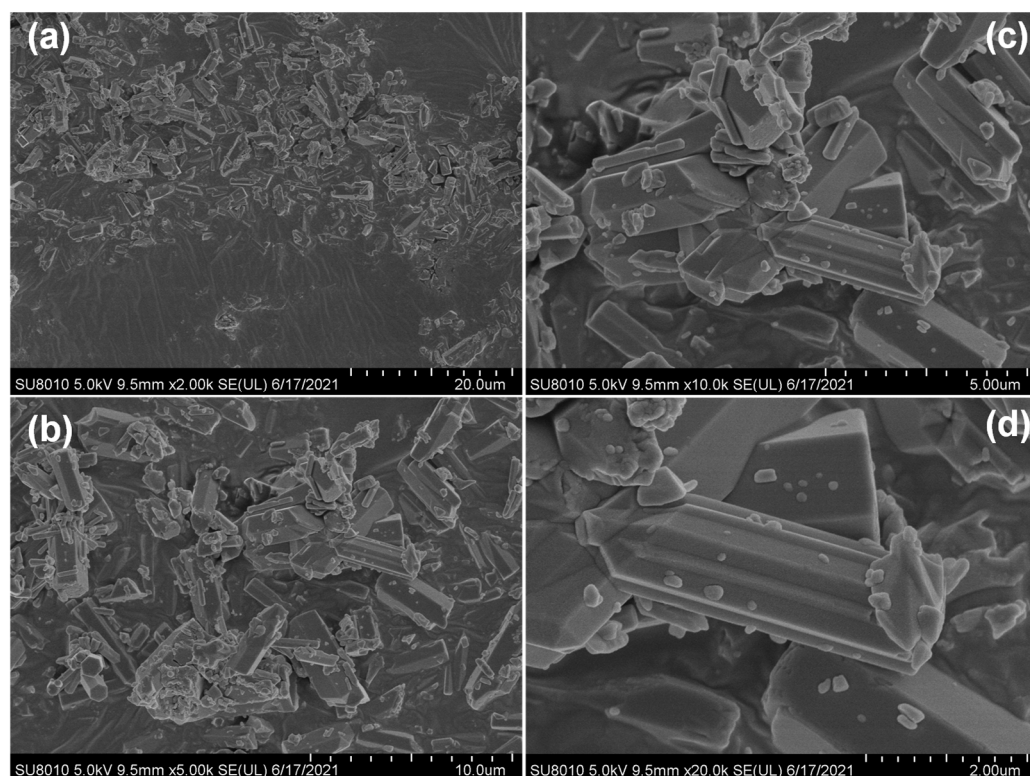


Figure 3. The scanning electron micrographs of WDM-ZnO at (a) 2.0k, (b) 5.0k, (c) 10.0k, and (d) 20.0k magnifications.

Table 1. The microstructural parameters of the synthesized materials.

Synthesized Material	2θ ($^\circ$) with Preferred Plane Orientation (hkl)	Interplanar Distance (d) (\AA)	Crystallite Size (D) (nm)	Micro-Strain (ϵ) (10^{-4})	Dislocation Density (δ) (10^{14} m^{-2})	Stacking Fault (SF) (10^{-3})
WO ₃	24.32 (200)	3.6569	38.5659	9.3839	6.7235	2.0927
MoO ₃	27.12 (021)	3.2853	65.6305	5.5142	2.3216	1.1689
WDM *	27.10 (021)	3.2877	63.1970	5.7265	2.5038	1.2143
ZnO	36.28 (101)	2.4741	36.3663	9.9515	7.5614	1.8515
WDM-ZnO	36.28 ^a (101)	2.4741	36.3663	9.9515	7.5614	1.8515
WDM-ZnO	27.10 ^b (021)	3.2877	62.2745	6.2274	2.5786	1.2323

* WDM is the short name given to WO₃-doped MoO₃. ^a Peak position of ZnO (101) plane in WDM-ZnO composite, ^b peak position of MoO₃ (021) plane in WDM-ZnO composite.

For pure MoO₃ and WDM, the diffraction pertaining to the plane orientation (021) was preferred to estimate the crystallite size of orthorhombic MoO₃ in pure MoO₃ and WDM. A decrease in crystallite size from 65.6305 nm (MoO₃) to 63.1970 nm (WDM) was noticed after the introduction of W⁶⁺ in the structure of MoO₃. Whereas a minor increase in the micro-strain, dislocation density, stacking fault, and interplanar distance was observed in WDM in comparison to pure MoO₃. These changes in microstructural properties and decrease in crystallite size of WDM reveal a minor disturbance in the MoO₃ lattice due to the introduction of W⁶⁺. Similar changes in the lattice of MoO₃ due to the incorporation of different dopants have been reported previously [27,29,30]. Moreover, the microstructural properties of the WDM-ZnO composite were also determined and compared with the properties of ZnO and WDM, as shown in Table 1. In contrast, a smaller crystallite size and a slight increase in other microstructural characteristics (Table 1) were

discernible in comparison to pure WDM, whereas no changes were seen in the properties of hexagonal ZnO.

In Figure 4, the absorption spectra of ZnO and its composite with WDM are contrasted. When compared to pure ZnO, the WDM-ZnO composite exhibits a reduction in UV light absorption and an increase in photon absorption in the visible area. This extended absorption response of the composite material is mainly due to the presence of Mo^{6+} - (major) and W^{6+} - (minor) based phases in the composite, whereas a mild shift in the absorption edge of ZnO to lower wavelength is attributed to the lowering of the ZnO conduction band ($3d^{10} 4s^0$), primarily by Mo^{6+} entities. The direct bandgap energies of pure ZnO and WDM-ZnO were calculated by plotting a graph of $(F(R) \times hv)^2$ against hv (eV) as shown in the inset of Figure 4. The bandgap energy evaluated for pure ZnO (~ 3.17 eV) was in good accord with literature assessments [31]. The dual different band energies were observed for WDM-ZnO in comparison to pure ZnO, which further supports the synthesized material's composite origin. In composite material, a ~ 3.14 eV bandgap energy was attributed to the ZnO component, whereas ~ 2.80 eV was due to the presence of WDM. A minor decrease in the bandgap energy of ZnO is observed due to the existence of WDM entities in the lower vicinity of the ZnO conduction band. The calculated bandgap energy for the WDM component in the composite was found to be between the bandgap energies of MoO_3 (~ 2.87 eV) and WO_3 (~ 2.74 eV).

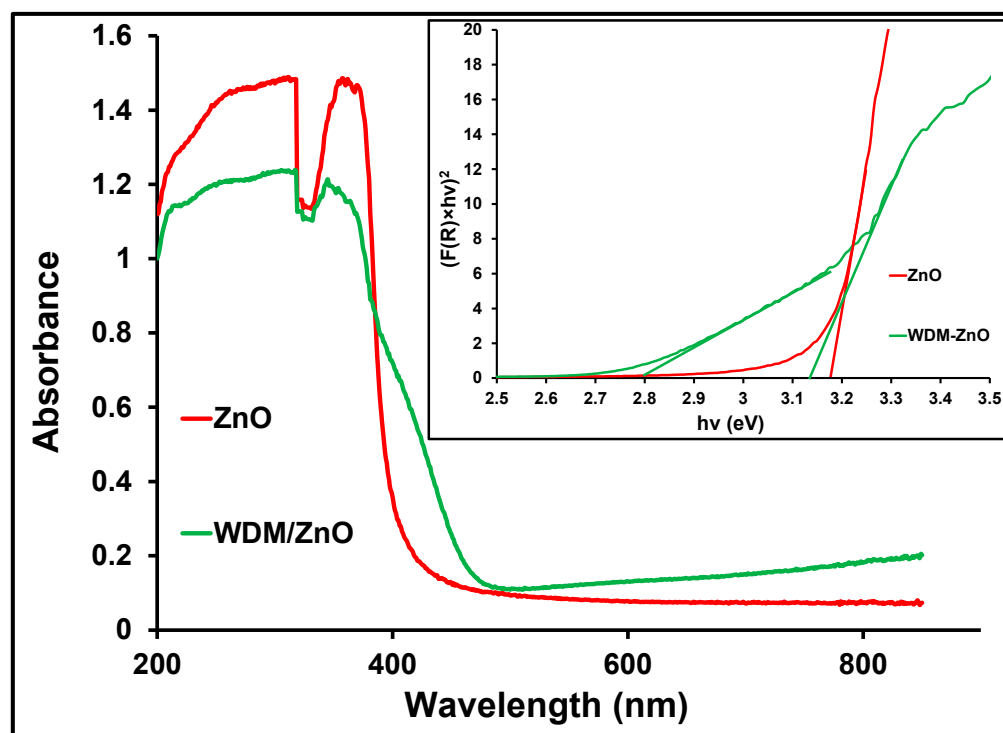


Figure 4. ZnO and WDM-ZnO composite solid-state absorption spectra are compared, and the inset shows a direct bandgap analysis of both photocatalysts.

In Figure 5, the photoluminescence (PL) spectra of WDM-modified ZnO and pure ZnO are contrasted. It is found that the emission intensity of WDM-ZnO is much lower than that of undoped ZnO. ZnO is a highly luminous substance whose relative greater emission intensity indicates increased electron–hole pair recombination, reducing its photocatalytic activity by limiting the production of ROS for the destruction of target pollutants [32]. Whereas, the newly synthesized WDM-ZnO composite showed a lower emission intensity, as shown in Figure 5, which ultimately led to the suppressing of $e^- - h^+$ recombination by extending their stay-time in respective bands. These excited species react with the O_2 and H_2O present in the photocatalytic system to produce a sufficient amount of ROS for further

degradation. Therefore, WDM-ZnO having a lower photoluminescence intensity shows greater photocatalytic activity than pure ZnO [33,34].

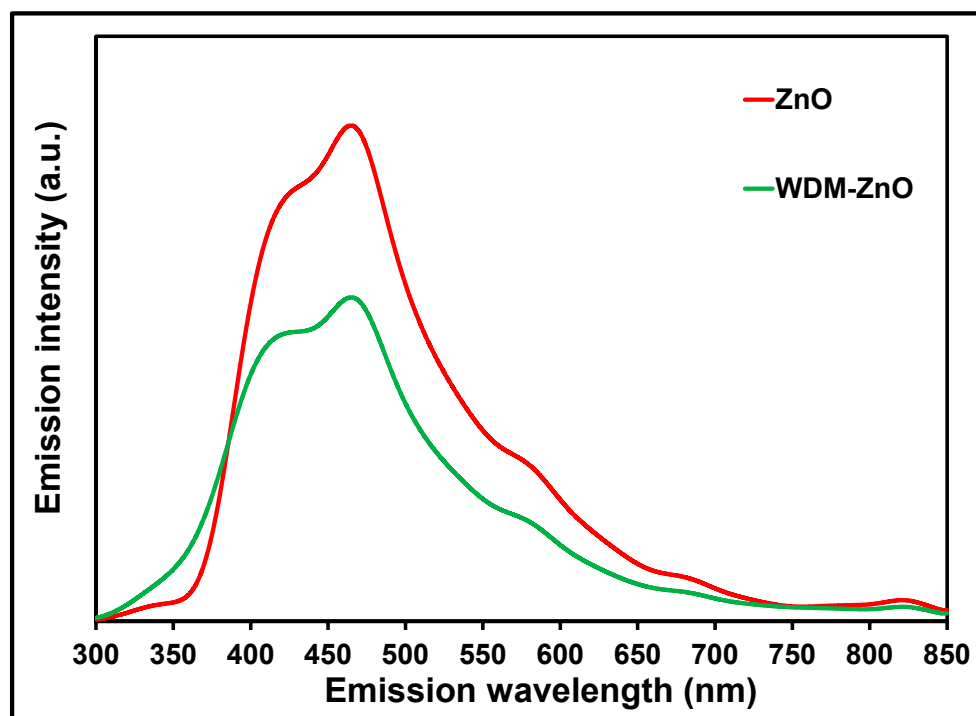


Figure 5. PL spectra of WDM-ZnO and ZnO photocatalysts are compared.

Under the irradiation of direct sunlight, ZnO and WDM-ZnO were investigated for their photocatalytic ability in the elimination of 2-NP. The absorption spectra of 2-NP samples that were obtained at various times of sunlight exposure were recorded in order to track the progression of substrate breakdown. Prior to the light exposure, dark testing was conducted to estimate the adsorption of 2-NP on the surface of both catalysts and the amounts of adsorption by the ZnO and WDM-ZnO materials were found to be ~2% and ~5%, respectively. The representative absorption spectra, as shown in Figure 6a,b, present a continuous decrease in 2-NP content with increasing natural sunlight exposure time over the ZnO and WDM-ZnO photocatalysts, respectively. The photocatalytic removal of 2-NP over the synthesized photocatalysts was calculated using the following Equation (5) [35].

$$\% \text{ removal} = \frac{C_o - C_t}{C_o} \times 100 \quad (5)$$

Here, C_o is the pollutant's initial concentration whereas C_t is the concentration of the pollutant after some light exposure time ' t '. The comparison of % removal of 2-NP by the synthesized photocatalysts with increasing exposure of natural sunlight is presented in Figure 6c. Wherein, a higher removal (~90%) of 2-NP was noticed due to the WDM-ZnO photocatalyst whereas ZnO was able to remove ~65% of 2-NP during the same sunlight exposure time. This higher removal of the 2-NP pollutant by WDM-ZnO in contrast to pure ZnO was attributed to its greater photon harvesting and lower electron-hole recombination [34–36]. Furthermore, using Equation (6) to assess the kinetics of the photocatalytic elimination of 2-NP under the exposure to light, the validity of the Langmuir–Hinshelwood (L-H) kinetic model was also investigated [35].

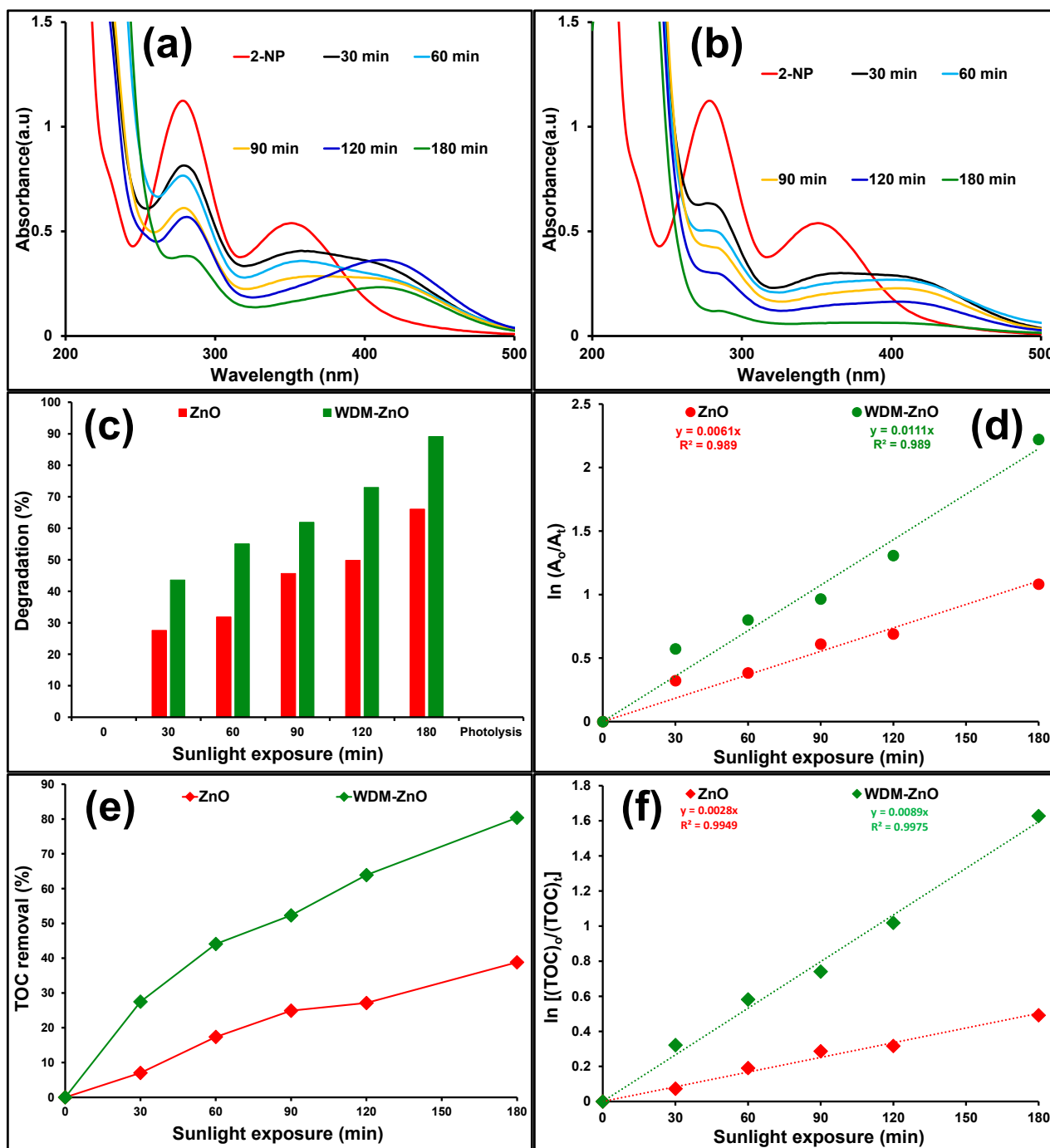


Figure 6. Comparison of (a,b) the decrease in absorption of 2-NP over (a) ZnO and (b) WDM-ZnO, (c) degradation (%), (d) rate of degradation, (e) TOC removal and (f) rate of TOC removal of 30 ppm 2-NP under the exposure of natural sunlight.

$$\ln \frac{C_0}{C_t} = k \times t \quad (6)$$

When $\ln \frac{C_0}{C_t}$ vs. t was plotted, the slope yielded the rate constant, k , which was then calculated. The kinetic analysis revealed that the photocatalytic removal of 2-NP over the produced photocatalysts followed the Langmuir–Hinshelwood (L-H) kinetic model, as illustrated in Figure 6d. Moreover, a higher 2-NP removal rate, i.e., $1.1 \times 10^{-2} \text{ min}^{-1}$, was noticed for WDM-ZnO in comparison to pure ZnO ($k = 6.1 \times 10^{-3} \text{ min}^{-1}$). Monitoring the

variations in total organic carbon (TOC) throughout the photocatalytic degradation process is highly recommended for the full removal of contaminants, since merely the degradation does not ensure the removal of all organic contents from the polluted water [36].

Figure 6e compares the removal of TOC from 2-NP by pure ZnO and WDM-ZnO. In contrast to ZnO, the synthesized WDM-ZnO photocatalyst removed more TOC from the 2-NP substrate. In the initial 30 min of sunlight exposure, ~27% of the TOC was removed by WDM-ZnO, whereas unmodified ZnO removed only ~7% of the TOC. The WDM-ZnO photocatalyst was able to remove ~80% of the TOC of 30 ppm 2-NP, whereas ~38% of the TOC was removed by pure ZnO in 180 min of sunlight exposure, as shown in Figure 6e. Moreover, the rate of TOC removal was also evaluated and is presented in Figure 6f. Wherein, a substantially higher TOC removal rate for WDM-ZnO than for pure ZnO was seen, which may be due to the successful usage of free-charge carriers (e^- and h^+ produced as a result of light illumination of WDM-ZnO) for the generation of ROS due to decreased e^- - h^+ recombination and the higher charge-transfer ability offered by WDM-ZnO (Figure 5). The estimation of the charge-transfer ability of the materials was assessed through a Nyquist plot using electrochemical impedance spectroscopy (EIS), as shown in Figure 7. The EIS spectra show a decrease in the semi-circle radius for WDM-ZnO as compared to unmodified ZnO, which implies that WDM-ZnO posed lower charge-transfer resistance than ZnO, which further verifies the increase in charge separation, and thus easy charge transfer, in WDM-ZnO [37].

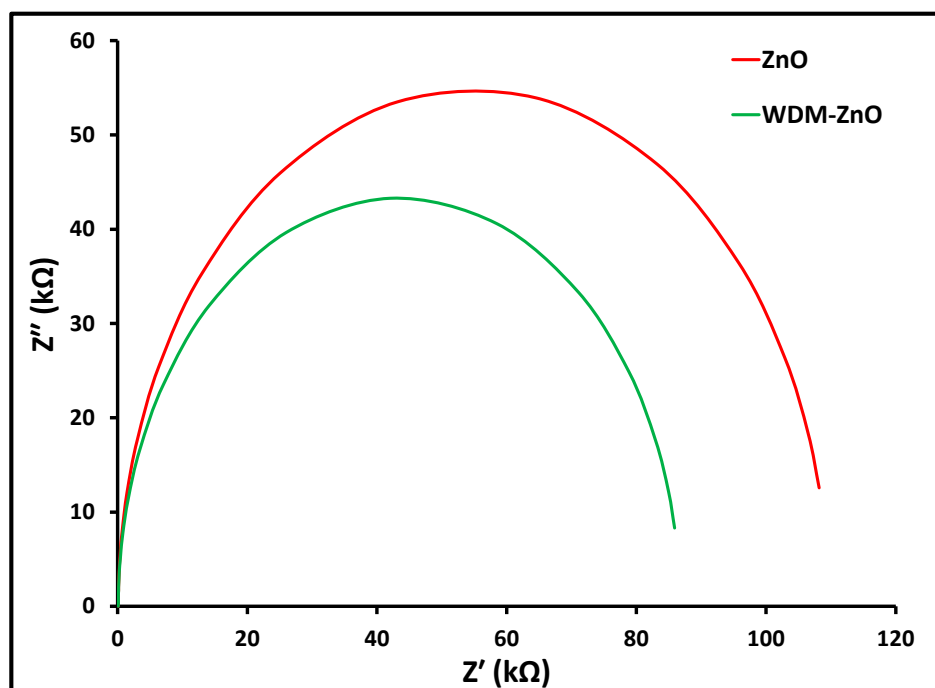


Figure 7. The comparison of EIS response of ZnO and WDM-ZnO photocatalysts.

It is reported that during photocatalysis, charge carriers such as electrons (e^-) and holes (h^+) are produced in the conduction band (CB) and valence band (VB), respectively, in a photocatalyst upon light irradiation. The photogenerated holes (h^+) oxidize water present in the photocatalytic system or hydroxyl ions adsorbed on the surface of the catalyst to generate hydroxyl free radicals ($\bullet\text{OH}$), whereas the photogenerated electrons interact with adsorbed oxygen molecules to produce superoxide anion radicals ($\text{O}_2^{\bullet-}$) [38,39]. These ROS, i.e., $\text{O}_2^{\bullet-}$ and $\bullet\text{OH}$, remove organic toxins. As the generation of ROS and their role in the oxidation of 2-NP is mainly based on the suitable potential of band-edges present in a

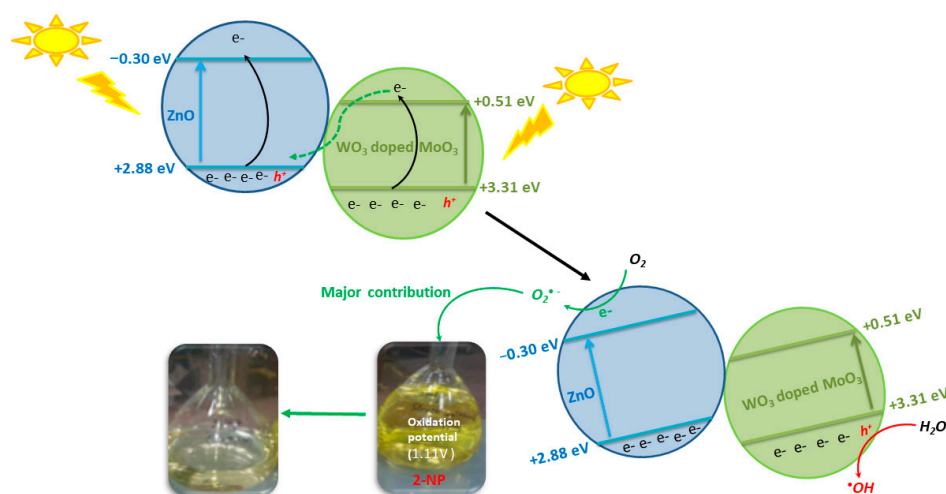
photocatalyst, therefore, the following equations have been used to calculate the band-edge potentials [40,41]:

$$E_{CB} = \chi - E^e - \frac{1}{2}E_g \quad (7)$$

$$E_{VB} = E_{CB} + E_g \quad (8)$$

where χ is the geometric mean of the absolute electronegativity of the constituent atoms, E^e is the energy of free electrons on the hydrogen scale (~ 4.5 eV), E_g is the photocatalyst's bandgap, E_{CB} is the conduction band potential, and E_{VB} is the valence band potential. Moreover, the Pearson absolute electronegativity values for Zn, Mo, W, and O were 4.45 eV, 3.90 eV, 4.40 eV, and 7.54 eV, respectively. The E_g values of ZnO and WDM estimated using a Tauc plot are 3.17 eV and 2.88 eV, respectively. As a result, the calculated conduction band energy (E_{CB}) values of ZnO and WDM are -0.30 eV and $+0.51$ eV, respectively, whereas the valence band energy (E_{VB}) values of ZnO and WDM are $+2.88$ eV and $+3.31$ eV, respectively.

As the photocatalytic process initiates upon the illumination of the WDM-ZnO composite with natural sunlight, both components of the photocatalyst generate electrons and holes, in their respective conduction and valence bands, of distinct band potentials. In addition, the potentials of these bands decide the fate of the photogenerated free-charge carriers. The calculated energy values of the respective bands indicate that the E_{CB} of ZnO is more negative than the reduction potential of O_2 to $O_2^{\bullet-}$ (-0.28 eV) [41]. Therefore, electrons in the CB of ZnO are capable of producing superoxide anion radicals, whereas the electrons in the CB of WDM cannot produce $O_2^{\bullet-}$ due to having a more positive CB potential than -0.28 eV. Moreover, the electrons in the CB of WDM transfer to the VB of ZnO while following the S-scheme of charge transfer and combine with holes residing there, as shown in Scheme 1. Finally, the system is left with electrons in the CB (-0.30 eV) of ZnO for $O_2^{\bullet-}$ generation and holes in the VB ($+3.31$ eV) of WDM for $\bullet OH$ generation. These ROS have a very short life and immediately react with the pollutant 2-NP, whose oxidation potential is ~ 1.11 eV against the standard hydrogen electrode (SHE) [42]. Furthermore, the valence band maximal positions of ZnO and WO_3 -doped MoO_3 were 2.88 and 3.31 eV, respectively, as shown by the VB XPS investigation (Figure 8).



Scheme 1. The plausible mechanism for the removal of 30 ppm 2-NP over WDM-ZnO photocatalyst under natural sunlight exposure.

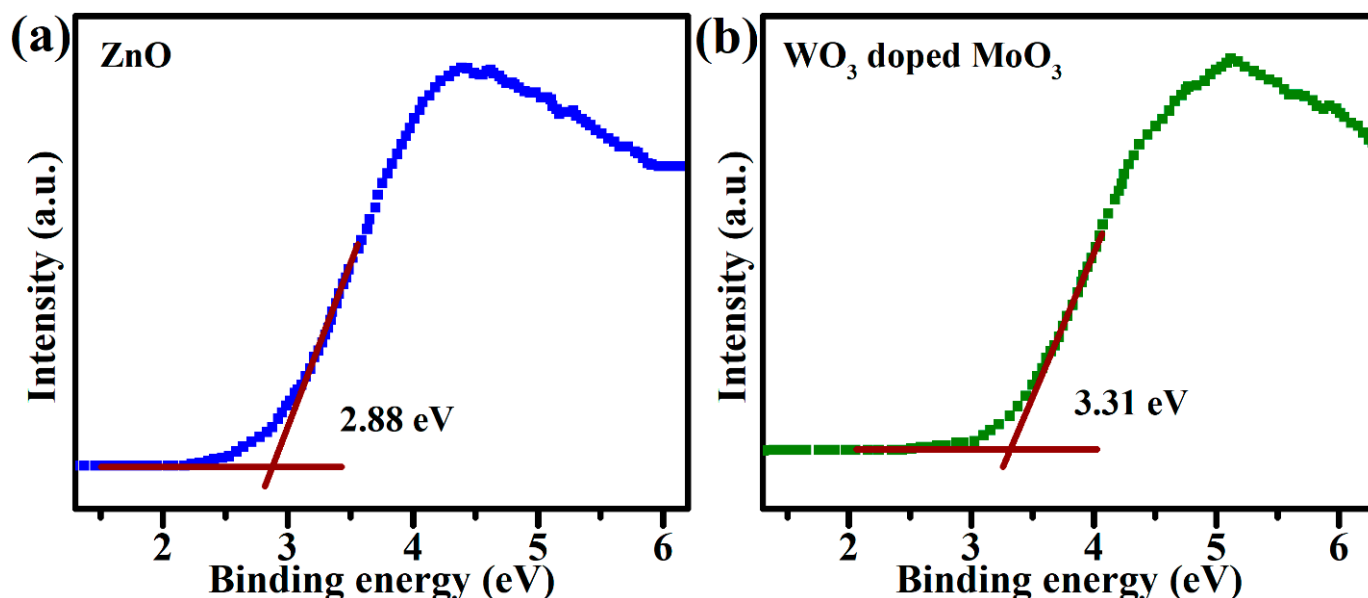


Figure 8. Valence band XPS spectra of (a) ZnO and (b) WO₃-doped MoO₃.

These ROS such as O₂^{•−} and •OH play a significant role in the removal of organic contaminants from polluted water; however, identifying the major contributor between these two ROS is very critical, which further helps in establishing the mechanism of degradation. In this context, two experiments related to the trapping of O₂^{•−} and •OH according to the reported method were conducted, wherein p-benzoquinone and isopropyl alcohol were added separately to the photocatalytic reaction containing WDM-ZnO and an aqueous solution of 30 ppm 2-NP to scavenge O₂^{•−} and •OH, respectively, produced because of the light illumination of WDM-ZnO [22,23]. The 2-NP removal (%) was calculated after 180 min of sunlight exposure as shown in Figure 9. The removal efficiency was reduced to ~22% and ~60% upon the addition of p-benzoquinone and isopropyl alcohol, respectively. This ROS-trapping investigation suggests that O₂[•] is mainly responsible for the photocatalytic removal of 2-NP over the WDM-ZnO photocatalyst when exposed to natural sunlight, however, the contribution of •OH cannot be totally discounted. Moreover, the following equations can also explain the mechanism for the photocatalytic removal of 2-NP by WDM-ZnO under the illumination of natural sunlight:



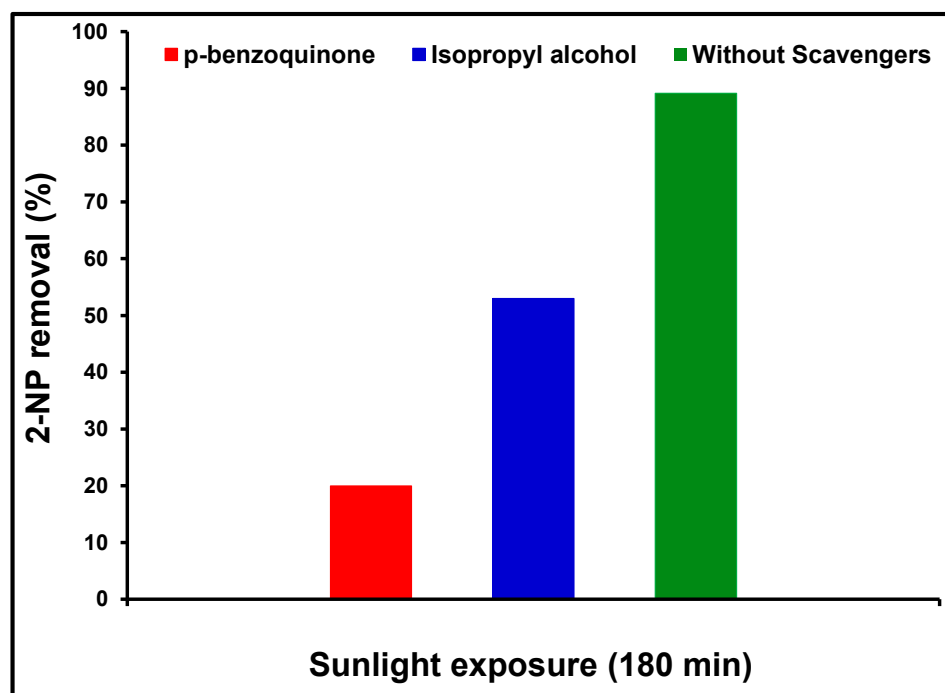


Figure 9. The effect of scavengers on the photocatalytic removal of 30 ppm 2-NP over WDM-ZnO photocatalyst under the illumination of natural sunlight.

The reusability of the WDM-ZnO photocatalyst was assessed in three different cycles with an interval of 24 h by estimating the degradation (%) of the fresh substrate (30 ppm 2-NP) under similar conditions to the photocatalytic experiment. The results revealed a ~7% lower efficiency of WDM-ZnO after the third cycle in comparison to the use of the fresh photocatalyst, as shown in Figure 10.

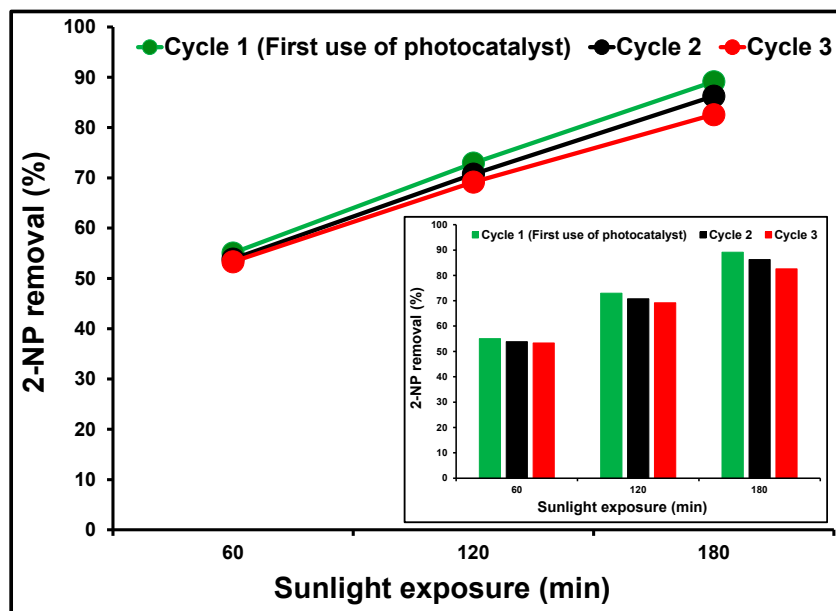


Figure 10. Comparison of reusability of WDM-ZnO for the photocatalytic removal of 30 ppm 2-NP under the illumination of natural sunlight.

3. Experimental

3.1. Surfactant-Assisted Synthesis of WO_3 , MoO_3 , and ZnO

In a typical WO_3 synthesis, 100 mL of distilled water were used to dissolve 5.00 g of $Na_2WO_4 \cdot 2H_2O$ (VWR, Radnor, PA, USA). A clear solution was produced by continuous stirring, and 3 mL of TX-100 (surfactant) was then added to the solution while it was still being swirled. HNO_3 was gradually added to the solution containing W^{6+} until a yellow precipitate was produced. The precipitate was cleaned using distilled water, a solution of ethanol, and acetone, and Whatman filter paper. The precipitate underwent further drying for 10 h at 100 °C in a hot air oven. In a Vulcan D-550 muffle furnace at 500 °C for four hours, the dry product was ground up and calcined. The calcined yellow powder was then placed in a glass vial and labeled " WO_3 ". For the synthesis of MoO_3 , 30.00 g of $(NH_4)_6Mo_7O_{24} \cdot 4H_2O$ was dissolved in 100 mL of distilled water at 50 °C while being continuously stirred until fully dissolved. This was performed before adding 3 mL of TX-100 as a surfactant. The combination of surfactant and Mo^{6+} was hydrolyzed by adding HNO_3 gradually until a precipitate that was grey and white formed. After using Whatman filter paper to separate the precipitate, it was cleaned with distilled water and an ethanol and acetone solution before being dried for 10 h in a 100 °C oven. The dried precipitate was crushed and calcined for four hours at 500 °C in a Vulcan D-550 muffle furnace. In a glass vial, the resulting powder was kept as MoO_3 .

$Zn(NO_3)_2 \cdot 6H_2O$ (Sigma-Aldrich, Taufkirchen, Germany) was fully dissolved in 100 mL of distilled water at 50 °C with constant stirring to produce ZnO . After the precursor had completely dissolved, 3 mL of the surfactant TX-100 was inserted, and the mixture was rapidly agitated at 50 °C. KOH was slowly added to the mixture that included surfactants, hydrolyzing it until an off-white precipitate formed. The precipitate was then filtered using Whatman filter paper and rinsed with distilled water, ethanol, and acetone to remove the surfactant and alkali components. Before being ground into powder, the precipitate was dried for 8 h at 100 °C in an oven. The powder was calcined in a Vulcan D-550 muffle furnace for four hours at 500 °C to produce white-colored calcined ZnO , which was then kept as ZnO in a glass vial.

3.2. Synthesis of WO_3 Doped MoO_3 and WDM- ZnO Composite

In this typical synthesis, 32.20 g $(NH_4)_6Mo_7O_{24} \cdot 4H_2O$ (Sigma-Aldrich, Taufkirchen, Germany) and 0.50 g $Na_2WO_4 \cdot 2H_2O$ (VWR, Radnor, PA, USA) were dissolved completely in distilled water in two separate beakers A and B, respectively. Triton X-100 (3 mL) was added as a surfactant after the solutions (A and B) had been well mixed while being continuously stirred at 50 °C. The combination of surfactant, W^{6+} , and Mo^{6+} was hydrolyzed by adding HNO_3 slowly until a yellowish-white precipitate at pH 2 was formed. The precipitate was then cleaned with an ethanol and acetone mixture, filtered using Whatman filter paper, and then washed first with distilled water. The precipitate was ground into a powder, dried for 10 h at 100 °C in an oven, and then calcined for 4 h at 500 °C in a Vulcan D-550 muffle furnace. After being calcined, the powder was placed in a glass vial and labeled WDM. Moreover, WDM- ZnO composite was prepared by mixing equal amounts of pre-synthesized WDM and ZnO using a mortar and pestle. The mixed sample was stored in a glass vial and marked WDM- ZnO composite.

3.3. Characterization of Materials

The preferred plane orientation found in each XRD pattern recorded from 2 (5–90°) using a Cu K radiation-source-equipped X'pert X-ray powder diffractometer (Philips PW 1398, Philips, The Netherlands) was used to determine the microstructural properties such as crystallite size (D), interplanar distance (d), micro-strain (ϵ), dislocation density, and stacking fault (SF) of the synthesized materials. SEM (Hitachi SU8010, Tokyo, Japan) was used to assess the morphology of the produced materials. Pure ZnO and WDM- ZnO composite solid-state absorption spectra were captured using a Perkin Elmer UV-visible DRS (Lambda 650, Waltham, MA, USA). Additionally, the Kubelka–Munk transformation

F(R) was used to evaluate the direct bandgap energy on percent R data by showing $(F(R)/hv)^2$ vs. hv (eV). A fluorescence spectrometer at 200 nm excitation wavelength was used to acquire the photoluminescence emission spectra of pure ZnO and the WDM-ZnO composite (RF-5301 PC, Shimadzu, Kyoto, Japan). Electrochemical impedance spectroscopy was employed using a multi-channel potentiostat (Bio-logic Science Instrument, Knoxville, TN, USA) with an EC lab (EIS).

3.4. Photocatalytic Study

For a predetermined period of daylight, from 10:00 a.m. to 13:00 p.m., without stirring, the photocatalytic removal of 30 ppm 2-nitrophenol (Sigma-Aldrich, Taufkirchen, Germany) was investigated. The ideal concentration of pure ZnO (150 mg) was suspended in 150 mL of an aqueous solution containing 30 ppm of 2-NP, and the mixture was stirred for 10 min. The suspension was placed into a 14 cm (diameter) by 2 cm (height) glass reactor, which was kept in the dark for 30 min, to establish the adsorption–desorption equilibrium between the catalysts and pollutant. After that, the glass reactor was kept in direct sunlight for an additional 30 min. After that, 30 min intervals of light exposure were used to collect the samples, which were subsequently filtered via a 0.20 μ m syringe filter. The filtered samples were then run through a UV–visible spectrophotometer (UV-1800, Shimadzu, Kyoto, Japan) to track the elimination of 2-NP while focusing on its absorbance at a certain wavelength, in this case 278 nm (λ_{max}). Also measured using a total carbon (TOC-VCPH, Shimadzu, Kyoto, Japan) analyzer was total organic carbon (TOC). The elimination of 30 ppm 2-NP over the produced WDM-ZnO composite was seen using the same process under comparable circumstances. For comparison, the removal of 2-NP without a photocatalyst (photolysis) on exposure to sunlight was also monitored. Moreover, the trapping of ROS, i.e., $O_2^{\bullet-}$ and $\bullet OH$ was also investigated according to the reported method under similar conditions to that of the photocatalysis in this study [43,44].

4. Conclusions

This study revealed the effectiveness of WO_3 -doped MoO_3 (WDM) in suppressing the electron (e^-) and hole (h^+) recombination, lowering the charge-transfer resistance, and improving the spectral response of pristine ZnO. The photocatalytic efficiency of ZnO was significantly enhanced because of its integration with WDM. WDM played an efficient role in the separation of photogenerated charge carriers such as electrons (e^-) and holes (h^+) in ZnO, which ultimately had sufficient time to react with H_2O and O_2 to produce ROS. The composite nature of WDM-ZnO was confirmed due to the presence of hexagonal ZnO and orthorhombic phases of WO_3 -doped MoO_3 in the XRD patterns and SEM images. According to the photocatalytic investigations, WDM-ZnO removed more 2-NP during natural sunlight exposure than pure ZnO. Additionally, ROS scavenging showed that $O_2^{\bullet-}$ species contributed much more than $\bullet OH$ to the photocatalytic elimination of 2-NP when exposed to natural sunlight.

Author Contributions: Conceptualization, writing-original draft Preparation, S.M. and R.N.; methodology, software, acquisition of data, formal analysis, supervision, M.T.Q. and S.I.; validation, performed major experimental works, S.A., M.A. and M.R.; reviewed the original manuscript, acquisition of funding and critical revision, N.S.A. and H.A.I. All authors have read and agreed to the published version of the manuscript.

Funding: The authors extend their appreciation to the Ministry of Education in KSA for funding this research work through the project number KKU-IFP2-P-5.

Data Availability Statement: The datasets generated during and/or analyzed during the current study are available from the corresponding author upon reasonable request.

Acknowledgments: The authors extend their appreciation to the Ministry of Education in KSA for funding this research work through the project number KKU-IFP2-P-5.

Conflicts of Interest: The authors declare no conflict of interest.

References

1. Johnson, A.C.; Jin, X.; Nakada, N.; Sumpter, J.P. Learning from the past and considering the future of chemicals in the environment. *Science* **2020**, *367*, 384–387. [PubMed]
2. Varjani, S.; Rakholiya, P.; Ng, H.Y.; You, S.; Teixeira, J.A. Microbial degradation of dyes: An overview. *Bioresour. Technol.* **2020**, *314*, 123728. [PubMed]
3. Wang, X.; Jiang, J.; Gao, W. Reviewing textile wastewater produced by industries: Characteristics, environmental impacts, and treatment strategies. *Water Sci. Technol.* **2022**, *85*, 2076–2096.
4. Ardila-Leal, L.D.; Poutou-Piñales, R.A.; Pedroza-Rodríguez, A.M.; Quevedo-Hidalgo, B.E. A brief history of colour, the environmental impact of synthetic dyes and removal by using laccases. *Molecules* **2021**, *26*, 3813. [PubMed]
5. Collivignarelli, M.C.; Abbà, A.; Miino, M.C.; Damiani, S. Treatments for color removal from wastewater: State of the art. *J. Environ. Manag.* **2019**, *236*, 727–745.
6. Xiong, Z.; Zhang, H.; Zhang, W.; Lai, B.; Yao, G. Removal of nitrophenols and their derivatives by chemical redox: A review. *Chem. Eng. J.* **2019**, *359*, 13–31.
7. Deng, F.; Zhang, Q.; Yang, L.; Luo, X.; Wang, A.; Luo, S.; Dionysiou, D.D. Visible-light-responsive graphene-functionalized Bi-bridge Z-scheme black BiOCl/Bi₂O₃ heterojunction with oxygen vacancy and multiple charge transfer channels for efficient photocatalytic degradation of 2-nitrophenol and industrial wastewater treatment. *Appl. Catal. B Environ.* **2018**, *238*, 61–69.
8. Balakrishnan, A.; Gaware, G.; Chinthala, M. Heterojunction photocatalysts for the removal of nitrophenol: A systematic review. *Chemosphere* **2022**, *310*, 136853.
9. Sathya, K.; Nagarajan, K.; Carlin Geor Malar, G.; Rajalakshmi, S.; Raja Lakshmi, P. A comprehensive review on comparison among effluent treatment methods and modern methods of treatment of industrial wastewater effluent from different sources. *Appl. Water Sci.* **2022**, *12*, 70.
10. Nagda, A.; Meena, M.; Shah, M.P. Bioremediation of industrial effluents: A synergistic approach. *J. Basic Microbiol.* **2022**, *62*, 395–414.
11. Rashed, M.N. Adsorption technique for the removal of organic pollutants from water and wastewater. *Org. Pollut. Monit. Risk Treat.* **2013**, *7*, 167–194.
12. Ghazal, H.; Koumaki, E.; Hoslett, J.; Malamis, S.; Katsou, E.; Barcelo, D.; Jouhara, H. Insights into current physical, chemical and hybrid technologies used for the treatment of wastewater contaminated with pharmaceuticals. *J. Clean. Prod.* **2022**, *361*, 132079.
13. Paumo, H.K.; Dalhatou, S.; Katata-Seru, L.M.; Kamdem, B.P.; Tijani, J.O.; Vishwanathan, V.; Kane, A.; Bahadur, I. TiO₂ assisted photocatalysts for degradation of emerging organic pollutants in water and wastewater. *J. Mol. Liq.* **2021**, *331*, 115458.
14. Quddus, F.; Shah, A.; Iftikhar, F.J.; Shah, N.S.; Haleem, A. Environmentally Benign Nanoparticles for the Photocatalytic Degradation of Pharmaceutical Drugs. *Catalysts* **2023**, *13*, 511.
15. Alhogbi, B.G.; Aslam, M.; Hameed, A.; Qamar, M.T. The efficacy of Co₃O₄ loaded WO₃ sheets for the enhanced photocatalytic removal of 2, 4, 6-trichlorophenol in natural sunlight exposure. *J. Hazard. Mater.* **2020**, *397*, 122835. [PubMed]
16. Qamar, M.T.; Iqbal, S.; Aslam, M.; Alhujaily, A.; Bilal, A.; Rizwan, K.; Farooq, H.M.U.; Sheikh, T.A.; Bahadur, A.; Awwad, N.S. Transition metal doped CeO₂ for photocatalytic removal of 2-chlorophenol in the exposure of indoor white light and antifungal activity. *Front. Chem.* **2023**, *11*, 1126171.
17. Krishnan, A.; Swarnalal, A.; Das, D.; Krishnan, M.; Saji, V.S.; Shibli, S. A review on transition metal oxides based photocatalysts for degradation of synthetic organic pollutants. *J. Environ. Sci.* **2023**, *139*, 389–417.
18. Singh, K.; Kaur, H.; Sharma, P.K.; Singh, G.; Singh, J. ZnO and cobalt decorated ZnO NPs: Synthesis, photocatalysis and antimicrobial applications. *Chemosphere* **2023**, *313*, 137322.
19. Aslam, M.; Ismail, I.M.; Salah, N.; Chandrasekaran, S.; Qamar, M.T.; Hameed, A. Evaluation of sunlight induced structural changes and their effect on the photocatalytic activity of V₂O₅ for the degradation of phenols. *J. Hazard. Mater.* **2015**, *286*, 127–135. [PubMed]
20. Le, A.T.; Duy, H.L.T.; Cheong, K.-Y.; Pung, S.-Y. Immobilization of zinc oxide-based photocatalysts for organic pollutant degradation: A review. *J. Environ. Chem. Eng.* **2022**, *10*, 108505.
21. Dhiman, P.; Rana, G.; Kumar, A.; Sharma, G.; Vo, D.-V.N.; Naushad, M. ZnO-based heterostructures as photocatalysts for hydrogen generation and depollution: A review. *Environ. Chem. Lett.* **2022**, *20*, 1047–1081.
22. Phuruangrat, A.; Thongtem, S.; Thongtem, T. Hydrothermal synthesis, characterization, and photocatalytic performance of W-doped MoO₃ nanobelts. *Res. Chem. Intermed.* **2016**, *42*, 7487–7499. [CrossRef]
23. Mohammadi, M.; Negreiros, F.R.; Radlinger, T.; Edelmayer, P.; Netzer, F.P.; Surnev, S. Interaction of Na with 2D WO₃ and MoO₃ Layers on Pd (100): From Doping to 2D Bronze Formation. *J. Phys. Chem. C* **2022**, *126*, 3289–3300. [CrossRef]
24. Klinbumrung, A.; Thongtem, T.; Thongtem, S. Characterization of orthorhombic α-MoO₃ microplates produced by a microwave plasma process. *J. Nanomater.* **2012**, *2012*, 930763. [CrossRef]
25. Gao, P.; Ru, Q.; Pan, Z.; Zhang, J.; Xu, W.; Ling, F.C.-C.; Wei, L. Robust hetero-MoO₃/MoO₂@ N-doped carbon nanobelts decorated with oxygen deficiencies as high-performance anodes for potassium/sodium storage. *J. Colloid Interface Sci.* **2021**, *599*, 730–740. [PubMed]
26. Guo, M.; Luo, N.; Chen, Y.; Fan, Y.; Wang, X.; Xu, J. Fast-response MEMS xylene gas sensor based on CuO/WO₃ hierarchical structure. *J. Hazard. Mater.* **2022**, *429*, 127471.

27. Layegh, M.; Ghodsi, F.; Hadipour, H. Improving the electrochemical response of nanostructured MoO₃ electrodes by Co doping: Synthesis and characterization. *J. Phys. Chem. Solids* **2018**, *121*, 375–385.
28. Sen, S.K.; Dutta, S.; Khan, M.R.; Manir, M.; Dutta, S.; Al Mortuza, A.; Razia, S.; Hakim, M. Characterization and antibacterial activity study of hydrothermally synthesized h-MoO₃ nanorods and α -MoO₃ nanoplates. *Bionanoscience* **2019**, *9*, 873–882.
29. Balaji, M.; Chandrasekaran, J.; Raja, M.; Rajesh, S. Structural, optical and electrical properties of Ru doped MoO₃ thin films and its P–N diode application by JNS pyrolysis technique. *J. Mater. Sci. Mater. Electron.* **2016**, *27*, 11646–11658.
30. Yan, Y.; Li, S.; Yuan, B.; Hu, R.; Yang, L.; Liu, J.; Liu, J.; Wang, Y.; Luo, Z.; Ying, H. Flowerlike Ti-doped MoO₃ conductive anode fabricated by a novel NiTi dealloying method: Greatly enhanced reversibility of the conversion and intercalation reaction. *ACS Appl. Mater. Interfaces* **2020**, *12*, 8240–8248. [[CrossRef](#)]
31. Navarra, W.; Ritacco, I.; Sacco, O.; Caporaso, L.; Farnesi Camellone, M.; Venditto, V.; Vaiano, V. Density functional theory study and photocatalytic activity of ZnO/N-doped TiO₂ heterojunctions. *J. Phys. Chem. C* **2022**, *126*, 7000–7011. [[CrossRef](#)]
32. Sun, Y.; Zhang, W.; Li, Q.; Liu, H.; Wang, X. Preparations and applications of zinc oxide based photocatalytic materials. *Adv. Sens. Energy Mater.* **2023**, *2*, 100069. [[CrossRef](#)]
33. Geng, Y.; Li, N.; Ma, J.; Sun, Z. Preparation, characterization and photocatalytic properties of BiOBr/ZnO composites. *J. Energy Chem.* **2017**, *26*, 416–421. [[CrossRef](#)]
34. Pan, L.; Shen, G.-Q.; Zhang, J.-W.; Wei, X.-C.; Wang, L.; Zou, J.-J.; Zhang, X. TiO₂–ZnO composite sphere decorated with ZnO clusters for effective charge isolation in photocatalysis. *Ind. Eng. Chem. Res.* **2015**, *54*, 7226–7232. [[CrossRef](#)]
35. Kadam, V.V.; Shanmugam, S.D.; Ettiyappan, J.P.; Balakrishnan, R.M. Photocatalytic degradation of p-nitrophenol using biologically synthesized ZnO nanoparticles. *Environ. Sci. Pollut. Res.* **2021**, *28*, 12119–12130. [[CrossRef](#)]
36. Qamar, M.T.; Aslam, M.; Rehan, Z.; Soomro, M.T.; Basahi, J.M.; Ismail, I.M.; Almeelbi, T.; Hameed, A. The influence of p-type Mn₃O₄ nanostructures on the photocatalytic activity of ZnO for the removal of bromo and chlorophenol in natural sunlight exposure. *Appl. Catal. B Environ.* **2017**, *201*, 105–118. [[CrossRef](#)]
37. Luo, J.; Dai, Z.; Feng, M.; Gu, M.; Xie, Y. Graphitic carbon nitride/ferroferric oxide/reduced graphene oxide nanocomposite as highly active visible light photocatalyst. *Nano Res.* **2023**, *16*, 371–376. [[CrossRef](#)]
38. Nadikatla, S.K.; Chintada, V.B.; Gurugubelli, T.R.; Koutavarapu, R. Review of Recent Developments in the Fabrication of ZnO/CdS Heterostructure Photocatalysts for Degradation of Organic Pollutants and Hydrogen Production. *Molecules* **2023**, *28*, 4277. [[CrossRef](#)]
39. Bano, K.; Kaushal, S.; Kumar, A.; Singh, P. Sunlight-driven photocatalytic degradation of 4-nitrophenol and adsorptive removal of Mn (II) ions from industrial wastewater by biogenic synthesized CuO/SnO₂ heterojunction. *Mater. Today Chem.* **2022**, *26*, 101193. [[CrossRef](#)]
40. Cao, Q.; Li, Q.; Pi, Z.; Zhang, J.; Sun, L.-W.; Xu, J.; Cao, Y.; Cheng, J.; Bian, Y. Metal–organic-framework-derived ball-flower-like porous Co₃O₄/Fe₂O₃ heterostructure with enhanced visible-light-driven photocatalytic activity. *Nanomaterials* **2022**, *12*, 904. [[CrossRef](#)] [[PubMed](#)]
41. Alnaggar, G.; Alkanad, K.; Chandrashekar, S.S.G.; Bajiri, M.A.; Drmosh, Q.A.; Krishnappagowda, L.N.; Ananda, S. Rational design of a 2D TiO₂–MoO₃ step-scheme heterostructure for boosted photocatalytic overall water splitting. *New J. Chem.* **2022**, *46*, 9629–9640. [[CrossRef](#)]
42. Khani, M.; Sammynaiken, R.; Wilson, L.D. Electrocatalytic Oxidation of Nitrophenols via Ag Nanoparticles Supported on Citric-Acid-Modified Polyaniline. *Catalysts* **2023**, *13*, 465. [[CrossRef](#)]
43. Tan, J.; Wei, G.; Wang, Z.; Su, H.; Liu, L.; Li, C.; Bian, J. Application of Zn_{1-x}Cd_xS photocatalyst for degradation of 2-CP and TC, catalytic mechanism. *Catalysts* **2022**, *12*, 1100. [[CrossRef](#)]
44. Lee, Y.-J.; Kang, J.-K.; Park, S.-J.; Lee, C.-G.; Moon, J.-K.; Alvarez, P.J. Photocatalytic degradation of neonicotinoid insecticides using sulfate-doped Ag₃PO₄ with enhanced visible light activity. *Chem. Eng. J.* **2020**, *402*, 126183. [[CrossRef](#)]

Disclaimer/Publisher’s Note: The statements, opinions and data contained in all publications are solely those of the individual author(s) and contributor(s) and not of MDPI and/or the editor(s). MDPI and/or the editor(s) disclaim responsibility for any injury to people or property resulting from any ideas, methods, instructions or products referred to in the content.